Modeling vibrating panels excited by a non-homogeneous turbulent boundary layer

Corentin Guillon, Laurent Maxit, Emmanuel Redon

Modeling vibrating panels excited by a non-homogeneous turbulent boundary layer

Corentin Guillon[a], Laurent Maxit[a], Emmanuel Redon[a,b]

Accepté dans le J. of Fluids and Struct. le 16 août 2021

[a] Univ Lyon, INSA Lyon, LVA, 25 bis av. Jean Capelle, F-69621, Villeurbanne Cedex, France
[b] Université de Bourgogne, ESIREM, 9 av. Alain Savary, BP 47870, F-21078 Dijon, France

Abstract Predicting the vibration response of an elastic structure excited by a turbulent flow is of interest for the civil and military transportation sector. The models proposed in the literature are generally based on the assumption that the turbulent boundary layer (noted TBL in the following) exciting the structure is spatially homogeneous. However, this assumption is not always fulfilled in practice, in particular when the excited area is close to the starting point of the TBL or with curved structures. To overcome this issue, this work proposes to extend two approaches generally used for dealing with homogeneous TBL, namely the spatial and the wavenumber approaches. The extension of the spatial approach to non-homogeneous excitation is relatively straightforward and gives us a reference, however with costly computation. On the contrary, extending the wavenumber approach requires more developments and assumptions that have led the authors to develop a sub-area decomposition technique (SDT). It consists in partitioning the excited area in several sub-areas, assuming a homogeneous TBL pressure field on each sub-area and neglecting certain interactions between the sub-areas. A criterion on the sub-area size as a function of the minimum wavelength of the wall pressure field is proposed on the basis of the numerical calculations. A test case on a plate with varying thickness and excited by a growing TBL allows us to highlight: (1) the interest of the SDT compared to a classical calculation considering a homogeneous TBL; (2) the efficiency of the SDT in terms of computing time compared to the spatial approach.

1 Introduction

For a vehicle moving inside a fluid, the elastic structures forming the body may vibrate due to the pressure fluctuations on the exterior wall related to the turbulent boundary layer (TBL) that develops on their surface. These vibrations can cause disturbing noise or accelerate structure wear. In the case of military vessels and submarines in particular, noise radiated by the hull can be spotted by enemy sonars and reveal their position. It is necessary to have models that predict the vibrations of structures excited by random turbulent pressures in an early design stage, so as to develop new tools to minimize these vibrations. In this article, we will focus on taking the non-homogeneous TBL into account in the vibroacoustic model. Rectangular flat plates will be considered for this study.

When an elastic structure is set in a flow, a TBL appears on its surface. Turbulences are convected at convective velocity U_c, which varies between 0.6 and 0.8 times the flow speed. U_c is linked to the size of the structures within the TBL and therefore depends on TBL parameters and frequency (Salze et al., 2014; Arguillat et al., 2005; Smol'yakov, 2006). In the wavenumber domain, the energy is concentrated around the convective wavenumber $k_c = \omega/U_c$, where ω is the angular pulsation. Elastic panels respond essentially to the pressure fluctuations characterized by wavenumbers below the panel flexural wavenumber k_f. When ω increases, the convective wavenumber k_c moves in the high-wavenumber region, further away from k_f, and the main contributing part becomes the low-wavenumber region of the spectrum. Well above

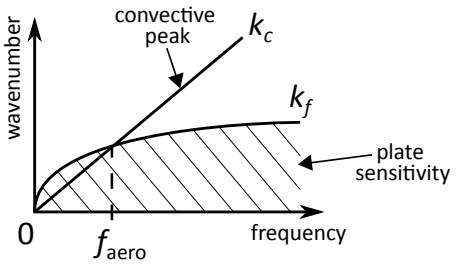

Figure 1: Plot on the wavenumber-frequency domain of k_c, k_f and f_{aero}.

the aerodynamic coincidence frequency f_{aero} (where $k_c = k_f$) panels behave like low wavenumber filters. Wavenumbers k_f and k_c are represented in a frequency-wavenumber plane in Fig. 1.

The calculation processes described in the literature generally assume that the TBL is spatially homogeneous (Maury et al., 2002; Hambric et al., 2004; Ciappi et al., 2009; Maxit et al., 2015). For practical applications, this assumption is rarely met. The growth of the TBL from its starting point may be at the origin of significant inhomogeneity which can affect the vibration of the excited structure. The goal of the present paper is to propose a calculation process taking into account inhomogeneity through the spatial variations of TBL parameters. Before introducing this process, let us look at how to model the exciting pressure under a TBL and different techniques for estimating the vibration response due to a homogeneous TBL.

The pressure under a homogeneous TBL is random and must be described with a cross-correlation function. The time-Fourier transform of this function gives the space-frequency wall pressure fluctuation (WPF) spectrum. The WPF spectrum is generally divided into two parts: firstly, the autospectrum that expresses the magnitude as a function of frequency, and secondly, the normalized cross-spectrum that contains the spatial correlation of the WPF. Using a spatial-Fourier transform, the cross-spectrum can be expressed in the wavenumber-frequency domain. Fig. 2 presents a schematic drawing of a typical WPF cross-spectrum in the wavenumber domain.

Concerning the autospectrum over a flat plate, Hwang et al. (2009) performed a comparative study of semi-empirical models: a dimensionless spectrum is given as a function of dimensionless frequency according to different scaling laws, depending on the frequency range (Ciappi and Magionesi, 2005; Ciappi et al., 2012). Goody (2004) suggested a semi-empirical model exploiting a wide variety of experimental pressure data for rigid flat plates set in air and water flows. The model contains a Reynolds-number dependent term, and can therefore be extrapolated to various flow conditions. However, vehicle structures are rarely flat and generally present a curvature which generates a pressure gradient. Schloemer (1967) showed that the pressure gradient has a strong influence on convective speed, confirmed by Magionesi et al. (2012). Rozenberg et al. (2012) proposed a Goody-inspired model that fits experimental data in the presence of an adverse pressure gradient.

The comparative study by Graham (1997), one of many references, presents several cross-spectrum models. The most common one is the Corcos model (Corcos, 1964), because (1) its simple expression can be easily transformed into both space and wavenumber domains; and (2) it depends on only two parameters. In the space domain, the decay of cross-correlation as a function of separation is described by an exponential profile that fits with the experimental observations (Salze et al., 2015). However, with the Corcos model, the coherence lengths of the WPF tend to infinite values in the low frequencies, which is not physically possible. The coherence lengths exhibit different behaviors over the frequency range (Palumbo, 2012) and some authors have proposed different models for these quantities (see for instance (Smol'yakov, 2006; Efimtsov, 1982)). Although it provides a good description of the convective peak, the Corcos model is known to overpredict spectrum levels by around 20 dB in the low-wavenumber region (Bonness et al., 2010). This model could be interpreted as a diamond shape window in the spatial domain; that is why Mellen (1990) suggested a

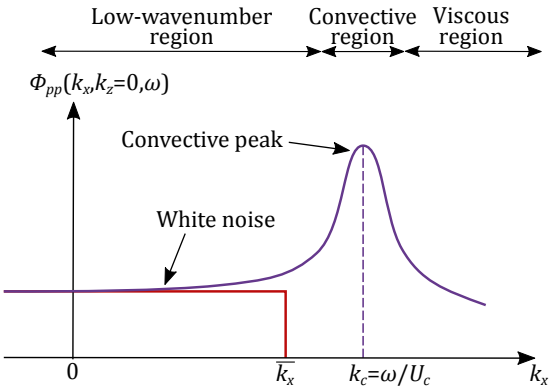

Figure 2: WPF wavenumber cross-spectrum.

Corcos-based model using a smooth elliptical window instead of the original angular shape. In the low wavenumber region, levels of the elliptical model drop by 8 dB from Corcos predictions. Another well-known model is the Chase model (Chase, 1980, 1987), but it is expressed in the wavenumber domain and its analytical expression cannot be transformed into the space domain. Additionally, it relies on many empirical parameters. Finnveden et al. (2005) showed that the value of the parameters given by Chase must be corrected depending on the case conditions, meaning this model needs a preliminary calibration study. A more recent model of interest is given by Caiazzo et al. (2016). They interpreted the Corcos model as a product of Butterworth filters of order one in complex space, and developed a "Generalized Corcos" model by changing the order of the filter along the streamwise direction from one to two. The levels predicted were 18 dB lower than those of the original Corcos model, but the convective peak was distorted, its shape becoming more rectangular when the filter order increased. While it tackles the issue of the Corcos model in the low-wavenumber region, this modification was based on mathematical rather than physical considerations.

Considering the low-wavenumber filtering effect, the key to choose a suitable cross-spectrum model is its behavior in the low wavenumber region, below the convective peak. Due to the dominant levels of the convective peak, measurement data in the low wavenumber region are difficult to obtain. However, in experimental set-ups where the flow conditions are controlled and where the vibrating structure is designed as a low wavenumber filter, so that the convective peak can be neglected, it is possible to derive exciting spectrum levels from vibrational behavior. Martin and Leehey (1977) implemented this inverse method with a rectangular membrane. Then Bonness et al. (2010) and Evans et al. (2013) used an aluminum cylindrical pipe excited by a water flow. Their measurements suggest that the low-wavenumber region of the WPF spectrum, between the acoustic and convective regions, is wavenumber-white, with a constant level for the normalized cross-spectrum.

The usual flow-induced vibrations calculation process is divided into 3 steps:

1. A hydrodynamic computation to obtain TBL parameters. The most popular method uses RANS (Reynolds-Averaged Navier-Stokes) equations, but under the condition that the Reynolds number is low enough, LES (Large Eddy Simulation) computation can be performed on a high-end machine (Cohen and Gloerfelt, 2018);

2. The TBL parameters are then used as input data in an appropriate semi-empirical WPF model described above;

3. A deterministic vibro-acoustic calculation gives the structure response to the WPF induced by the TBL.

The last step concerns the subject of this article. It consists in coupling a stochastic excitation model with a deterministic vibro-acoustic model. Several authors have studied different ways to achieve this coupling for spatially homogeneous TBL. Maxit et al. (2015) summarized five techniques for coupling stochastic TBL and deterministic vibro-acoustic structure models:

- The spatial method is based on a regular discretization of the excited surface. The discretization step must be substantially smaller than the convective wavelength $\lambda_c = 2\pi/k_c$ (Maxit et al., 2015), which gives a dense mesh, especially when the frequency increases, and therefore significant computing time. Franco et al. (2013) present three time saving approaches applied with FEM model. De Rosa and Franco (2008a,b) developed the scaled procedure ASMA, that gives a good approximation to the quadratic mean response while reducing calculation time.

- The Cholesky method uses a Cholesky decomposition of the matrix representation of the WPF space spectrum (Wittig and Sinha, 1975). The vibro-acoustic model is used to evaluate the panel response for several calculations of the random pressure fields. The Cholesky decomposition in itself is nonetheless time consuming and this method has the same drawback concerning mesh size.

- The wavenumber method allows interpreting the vibratory response as the WPF spectrum passing through a filter, this filter being the sensitivity function of the plate (Maury et al., 2002). Models may be made simpler well above the aerodynamic coincidence frequency, since the convective contributions of the WPF are negligible. Some spectra, like the Chase model, have an analytical expression in the wavenumber domain that cannot be transformed into the spatial domain.

- The previous method requires knowledge of the structure displacement response for harmonic plane waves. The Lyamshev reciprocity principle can be used to interpret the sensitivity functions as the plate point-response expressed in the wavenumber domain for a unit force (Fahy, 2003). The reciprocity method was used by Maxit et al. (2020) to calculate the sound radiated by a cylindrical shell. Marchetto et al. (2018) estimated a panel sensitivity function from measurements of velocity response when the plate was excited by mechanical forces instead of plane waves, using the reciprocity principle.

- Maxit (2016) showed that, in the wavenumber domain, the exciting WPF can be simulated with a set of uncorrelated wall plane waves (UWPW). The vibroacoustic response to this WPF is calculated with the modal expansion method, when the modal shapes and modal angular frequencies are known. The process is reiterated at each frequency for several random calculations of the pressure field. The definitive response is the average of the responses for all the calculations. Karimi et al. (2020) described a hybrid approach where the WPF obtained with the UWPW method is used as an input at the mesh points of an FEM of the structure.

For applications with large structures, for instance a ship hull, the TBL can be assumed fully developed with fairly constant parameters over a large part of the hull. However, for smaller structures, the fast growth from the tip can have an influence on the overall vibrational response. This paper proposes two methods to take the spatial variations of the TBL parameters into account in vibroacoustic coupling models. The first one is an adaptation of the spatial method whereas the second one, based on the wavenumber formulation, introduces the concepts of sub-area decomposition and sub-area sensitivity functions. The formulation in the wavenumber domain will preserve the interest of filtering the convective contributions that have a negligible effect on the vibrational response. Moreover, the surface excited by the TBL will be decomposed into sufficiently small sub-areas, allowing us to assume a homogeneous TBL on each sub-area and different types of assumptions concerning the interaction between the sub-areas. Using the methods proposed for describing the effect of a non-homogeneous TBL, the authors will use a test case to highlight the role of the spatially varying TBL parameters on vibrational levels.

The paper is organized as follows: section 2 recalls the space and wavenumber approaches for a structure excited by a homogeneous TBL. The issue of non-homogeneous TBL is then addressed in section 3. Subsection 3.1 shows how the spatial approach can be easily adapted to these cases. The results obtained will

Nomenclature

c_0	sound speed
D	plate flexural rigidity
E	Young's modulus
f_{aero}	aerodynamic coincidence frequency
h	plate thickness
H_v	frequency response function in velocity
$\hat{H}_v$	sensitivity function in velocity
$\hat{H}_{v,\zeta}$	sub-area sensitivity function
$\mathbf{k}$	wavevector
(k_x, k_z)	wavenumber in $\vec{x}$ and $\vec{z}$ directions
$(\bar{k}_x, \bar{k}_z)$	cutoff wavenumbers
k_c	convective wavenumber
k_f	flexural wavenumber
L_x	plate length
L_z	plate width
m, n	modal indices
$\mathbf{M}$	observation point
M_{mn}	modal mass
N	number of sub-areas
Re_x	Reynolds number
U_0	free flow speed
U_c	convective velocity
U_e	external velocity
u_τ	friction velocity
S_{pp}	WPF autospectrum
S_{vv}	vibration velocity autospectrum
W_{mn}	modal shape
$(\tilde{\mathbf{x}}, \tilde{\tilde{\mathbf{x}}})$	spatial variables of integration

Greek symbols

Γ_{pp}	WPF space frequency cross-spectrum
Δf	frequency step
δ	TBL thickness
$\delta k_x, \delta k_z$	wavenumber step
η	structural damping
λ_c	convective wavelength
λ_f	flexural wavelength
Λ_x, Λ_z	WPF mean coherence lengths
μ	wavenumber discretization parameter
ν	fluid kinematic velocity
ν_p	Poisson's ratio
ζ	sub-area indice
ξ	spatial separation
ρ	fluid density
ρ_p	plate material density
Σ	plate surface
τ	shear stress
Φ_{pp}	WPF wavevector frequency cross-spectr.
$\tilde{\Phi}_{pp}$	normalized WPF cross-spectrum
Ψ_{pp}	WPF cross-spectr. of a homogeneous TBL
ω	angular pulsation
ω_{mn}	modal pulsation
$\Omega_{\mathbf{k}}$	set of wavenumbers

Acronyms

FRF	frequency response function
SDT	sub-area decomposition technique
SF	sensitivity function
SMVA	spatial mean of the velocity autospectrum
TBL	turbulent boundary layer
WPF	wall pressure fluctuation

be considered in the following as references, but they require considerable computing time. An alternative method is then proposed in sub-section 3.2, the so-called sub-area decomposition technique related to the wavenumber formulation. Two types of assumptions between the sub-areas will be introduced. In section 4, a numerical study is carried out to evaluate the area of validity of the sub-area decomposition technique, with regard to the assumptions. It will lead to the definition of a criterion on the size of the sub-areas. The test cases are proposed in section 5, through three numerical applications with a plate of non-constant thickness excited by a growing TBL. The interest and limits of the approach proposed are discussed in the conclusion.

2 Flat plate excited by a homogeneous turbulent boundary layer

2.1 Formulation in the space domain

Let us consider a thin flat rectangular plate of surface Σ. The plate is placed in air and excited on one side by a turbulent flow in the $\vec{x}$ direction, while $\vec{y}$ orients the vertical axis and $\vec{z}$ the cross-stream direction. The fluid is characterized by a free flow speed U_0, a density ρ, a kinematic viscosity ν and a sound velocity c_0. Plate length and width are L_x in the streamwise direction and L_z in the crosswise direction respectively, as shown in Fig. 3. A TBL develops over the plate and the turbulences are convected under this TBL at speed U_c.

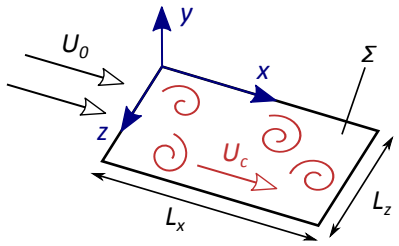

Figure 3: Flat plate model and axis orientation.

The TBL parameters are: the external velocity U_e, the boundary layer thickness δ and the wall shear stress τ. For a flat plate, two assumptions are made:

- the external velocity U_e is constant and equal to U_0;
- the pressure gradient is null.

In this part, the TBL is assumed stationary, spatially homogeneous and ergodic. We assume a weak coupling between the elastic plate and the fluid, which means the vibrations of the structure do not impact back on the TBL. Under this hypothesis, the plate is simply excited by the fluctuating wall pressure produced by the TBL on an infinitely rigid plate.

Let $\mathbf{M}$ be a point of the surface Σ and v the plate velocity response at this point. The autospectrum of the velocity response v is given by (Maury et al., 2002):

$$S_{vv}(\mathbf{M},\omega) = \iint_{\Sigma}\iint_{\Sigma} H_v(\mathbf{M},\tilde{\mathbf{x}},\omega)\Gamma_{pp}(\tilde{\mathbf{x}},\tilde{\tilde{\mathbf{x}}},\omega)H_v^*(\mathbf{M},\tilde{\tilde{\mathbf{x}}},\omega)\mathrm{d}\tilde{\mathbf{x}}\mathrm{d}\tilde{\tilde{\mathbf{x}}}, \tag{1}$$

where $H_v(\mathbf{M},\tilde{\mathbf{x}},\omega)$ is the frequency response function (FRF) in velocity at point $\mathbf{M}$ for a unit force applied at point $\tilde{\mathbf{x}}$ and $\Gamma_{pp}(\tilde{\mathbf{x}},\tilde{\tilde{\mathbf{x}}},\omega)$ is the WPF space-frequency cross-spectrum. The exponent * indicates the complex conjugate.

If the TBL is homogeneous, the WPF cross-spectrum function no longer depends on the position of the two points, but only on their spatial separation $\xi = \tilde{\tilde{\mathbf{x}}} - \tilde{\mathbf{x}}$. One can then write:

$$\Gamma_{pp}(\tilde{\mathbf{x}},\tilde{\tilde{\mathbf{x}}},\omega) = \Psi_{pp}(\tilde{\tilde{\mathbf{x}}} - \tilde{\mathbf{x}},\omega) = \Psi_{pp}(\xi,\omega),\ \forall\,(\tilde{\mathbf{x}},\tilde{\tilde{\mathbf{x}}}) \in (\Sigma\times\Sigma)\,, \tag{2}$$

where Ψ_{pp} is the WPF cross-spectrum of a homogeneous TBL.

Introducing Eq. (2) in Eq. (1) gives:

$$S_{vv}(\mathbf{M},\omega) = \iint_{\Sigma}\iint_{\Sigma} H_v(\mathbf{M},\tilde{\mathbf{x}},\omega)\Psi_{pp}(\xi,\omega)H_v^*(\mathbf{M},\tilde{\tilde{\mathbf{x}}},\omega)\mathrm{d}\tilde{\mathbf{x}}\mathrm{d}\tilde{\tilde{\mathbf{x}}}. \tag{3}$$

In practice, the 2-dimensional integrals are approximated by summations through a discretization of the plate area. $\mathbf{X_1}$ and $\mathbf{X_2}$ are the nodes of the spatial mesh, while δx and δz are the discretization steps in the $\vec{x}$ and $\vec{z}$ directions:

$$S_{vv}(\mathbf{M},\omega) \approx \sum_{\mathbf{X_1}} \sum_{\mathbf{X_2}} H_v(\mathbf{M},\mathbf{X_1},\omega)\Psi_{pp}(\mathbf{X_2}-\mathbf{X_1},\omega)H_v^*(\mathbf{M},\mathbf{X_2},\omega)\delta x^2 \delta z^2. \tag{4}$$

This expression permits evaluating S_{vv} at $\mathbf{M}$ from the cross-spectrum of the WPF expressed in the frequency-space domain and the velocity transfer functions between $\mathbf{M}$ and all the grid points of the discretization of the panel area.

2.2 Formulation in the wavenumber domain

Because of the double summation in Eq. (4), the spatial method is time consuming, especially for high frequencies where the convective length λ_c, which defines the finesse of the mesh, is small. It is then of interest to move into the wavenumber domain to drastically improve the algorithm speed.

Let us consider the WPF cross-spectrum in the wavenumber domain $\Phi_{pp}(\mathbf{k},\omega)$, defined as the spatial Fourier transform of $\Psi_{pp}(\xi,\omega)$. In Eq. (3), the cross-spectrum $\Psi_{pp}(\xi,\omega)$ is then replaced by:

$$\Psi_{pp}(\xi,\omega) = \frac{1}{(2\pi)^2} \iint_{\infty} \Phi_{pp}(\mathbf{k},\omega) e^{-i\mathbf{k}\cdot\xi} \mathrm{d}\mathbf{k}, \tag{5}$$

where i is the imaginary unit and $\mathbf{k} = (k_x, k_z)$ is the wavevector. One obtains (Maury et al., 2002; Maxit et al., 2015):

$$S_{vv}(\mathbf{M},\omega) = \frac{1}{4\pi^2} \iint_{\infty} \left|\hat{H}_v(\mathbf{M},\mathbf{k},\omega)\right|^2 \Phi_{pp}(\mathbf{k},\omega)\mathrm{d}\mathbf{k}, \tag{6}$$

where

$$\hat{H}_v(\mathbf{M},\mathbf{k},\omega) = \iint_{\Sigma} H_v(\mathbf{M},\tilde{\mathbf{x}},\omega) e^{i\mathbf{k}\cdot\tilde{\mathbf{x}}} \mathrm{d}\tilde{\mathbf{x}} \tag{7}$$

is called the sensitivity function (SF) and is the response in velocity at $\mathbf{M}$ when the plate of surface Σ is excited by a plane wave of wavevector $\mathbf{k}$.

By truncating the wavenumber domain to cutoff wavenumbers $(\bar{k}_x, \bar{k}_z)$ and discretizing it with a sampling resolution $(\delta k_x, \delta k_z)$, Eq. (6) is approximated by:

$$S_{vv}(\mathbf{M},\omega) = \frac{1}{4\pi^2} \sum_{\mathbf{k}\in\Omega_\mathbf{k}} \left|\hat{H}_v(\mathbf{M},\mathbf{k},\omega)\right|^2 \Phi_{pp}(\mathbf{k},\omega)\delta k_x \delta k_z, \tag{8}$$

where $\Omega_\mathbf{k}$ is the set of points in the truncated and discretized wavenumber domain. This expression presents only a single summation, compared to the double summation in Eq. (4).

Furthermore, in the wavenumber domain, it is possible to assimilate the plate as a low wavenumber filter for a more computationally efficient model for frequencies well above the aerodynamic coincidence frequency f_{aero}, say for frequencies above three times f_{aero}. Indeed, it is known that for these frequencies, the contributions of the convective peak of the WPF have a negligible effect on the panel response (Martin and Leehey, 1977).

In the following, the assumption that the contributions of the convective peak in Eq. (8) are negligible for the flow speed considered will be verified. The following criterion on the cutoff wavenumbers will be applied:

$$\bar{k}_x = \bar{k}_z = \mu k_f, \tag{9}$$

where μ is a coefficient between 1.1 and 1.8 and k_f is the flexural wavenumber. The role of μ is to delimit a domain of integration including the flexural wavenumber and excluding the convective wavenumber.

2.3 Analytical equations for a simply supported rectangular plate

In this sub-section, the calculation of the frequency response function and sensitivity function of the out-of-plane displacement of a rectangular plate is presented briefly, using the Kirchhoff-Love plate theory and modal expansion. Plate flexural rigidity is noted D, material density ρ_p and plate thickness h. For a simply supported rectangular plate, the modal wavenumbers k_m and k_n, the modal shape W_{mn}, the modal angular frequency ω_{mn}, the modal mass M_{mn} and the flexural wavenumber k_f are given respectively by:

$$k_m = \frac{m\pi}{L_x}\,, \quad k_n = \frac{n\pi}{L_z}\,, \tag{10}$$

$$W_{mn}(x,z) = \sin\left(xk_m\right)\sin\left(zk_n\right), \tag{11}$$

$$\omega_{mn} = \sqrt{\frac{D}{h\rho_p}}\left(k_m^2 + k_n^2\right)\,, \tag{12}$$

$$M_{mn} = \iint\limits_{\Sigma} h\rho_p W_{mn}^2(\tilde{\mathbf{x}})\mathrm{d}\tilde{\mathbf{x}} = h\rho_p\frac{L_xL_z}{4}\,, \tag{13}$$

$$k_f = \sqrt{\omega\sqrt{\frac{h\rho_p}{D}}}\,, \tag{14}$$

where the indices m and n designate the longitudinal and transverse modal order, respectively.

The FRF in velocity $H_v(\mathbf{M},\tilde{\mathbf{x}},\omega)$ used in the spatial approach (Eq. (4)) is given analytically by:

$$H_v(\mathbf{M},\tilde{\mathbf{x}},\omega) = \sum_{m,n}^{\infty}\frac{i\omega W_{mn}(\mathbf{M})W_{mn}(\tilde{\mathbf{x}})}{M_{mn}(\omega_{mn}^2 + i\eta\omega_{mn}\omega - \omega^2)}, \tag{15}$$

with η the structural damping.

Applying a Fourier transform over the space variable $\tilde{\mathbf{x}}$ on Eq. (15) gives the sensitivity function in the wavenumber approach (Eq. (8)):

$$\hat{H}_v(\mathbf{M},\mathbf{k},\omega) = \sum_{m,n}^{\infty}\frac{i\omega W_{mn}(\mathbf{M})\hat{W}_{mn}(\mathbf{k})}{M_{mn}(\omega_{mn}^2 + i\eta\omega_{mn}\omega - \omega^2)}, \tag{16}$$

where $\hat{W}_{mn}(\mathbf{k})$ is the Fourier transform of the shape $W_{mn}(\tilde{\mathbf{x}})$:

$$\hat{W}_{mn}(k_x,k_z) = \frac{k_mk_n}{\left(k_m^2 - k_x^2\right)\left(k_n^2 - k_z^2\right)}\left[(-1)^{m+1}\exp\left(iL_xk_x\right) + 1\right]\left[(-1)^{n+1}\exp\left(iL_zk_z\right) + 1\right]. \tag{17}$$

3 Spatially varying boundary layer

3.1 Varying TBL in the space domain

Let us assume that the TBL thickness δ and the shear stress τ depend on the spatial position x in the streamwise direction, while the TBL is invariant in the cross-stream direction $\vec{z}$. It can be seen that the cross-spectrum of the WPF between two points $\tilde{\mathbf{x}}$ and $\tilde{\tilde{\mathbf{x}}}$ does not depend only on their separation ξ (as supposed in section 2.1 with Eq. (2)). In Eq. (1), $\Gamma_{pp}(\tilde{\mathbf{x}},\tilde{\tilde{\mathbf{x}}},\omega)$ needs to be evaluated for a non-homogeneous TBL. LES calculation could provide this information but it requires considerable computing time (Cohen and Gloerfelt, 2018) and powerful machines. An alternative consists in making several assumptions in order to build this quantity from those defined separately at $\tilde{\mathbf{x}}$ and $\tilde{\tilde{\mathbf{x}}}$, considering the WPF for a homogeneous model.

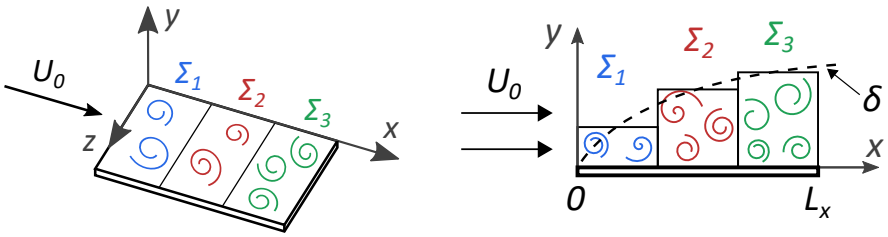

Figure 4: Surface Σ divided in 3 sub-areas and TBL discretization.

On one hand, the WPF of a TBL is weakly correlated spatially. The coherence lengths Λ_x and Λ_z in directions $\vec{x}$ and $\vec{z}$ of the cross-spectrum, explicitly defined in the Corcos and Mellen models, constitute a relevant indicator of the decay of spatial correlation. If the distance between the two points is typically greater than four times the coherence length, the cross-spectrum of the WPF $\Gamma_{pp}(\tilde{\mathbf{x}}, \tilde{\tilde{\mathbf{x}}})$ may be negligible.

On the other hand, for a TBL presenting relatively small variations of its parameters along less than four coherence lengths, the WPF around two points $\tilde{\mathbf{x}}$ and $\tilde{\tilde{\mathbf{x}}}$, whose separation is less than four times the coherence length, can be assumed to exhibit strong similarities. Hence, the cross-spectrum of the WPF $\bar{\Gamma}_{pp}(\tilde{\mathbf{x}}, \tilde{\tilde{\mathbf{x}}}, \omega)$ may be approximated by considering the spectrum calculated with an arithmetic mean of the TBL parameters at the 2 points.

For the Corcos and Mellen models, the coherence lengths in the streamwise and cross-wise directions are:

$$\Lambda_x(\omega) = \frac{U_c}{\alpha_x \omega} \quad \text{and} \quad \Lambda_z(\omega) = \frac{U_c}{\alpha_z \omega}\,, \tag{18}$$

where the two parameters $\alpha_x = 0.10$ and $\alpha_z = 0.77$ are the constants of the Corcos model.

For the Mellen elliptical model, these assumptions can be expressed by the following equation:

$$\Gamma_{pp}(\tilde{\mathbf{x}}, \tilde{\tilde{\mathbf{x}}}, \omega) = \begin{cases} \bar{\Gamma}_{pp}(\tilde{\mathbf{x}}, \tilde{\tilde{\mathbf{x}}}, \omega) & \text{, if } \|\tilde{\mathbf{x}} - \tilde{\tilde{\mathbf{x}}}\| < 4\sqrt{\Lambda_x(\omega)^2 + \Lambda_z(\omega)^2}, \\ 0 & \text{, if } \|\tilde{\mathbf{x}} - \tilde{\tilde{\mathbf{x}}}\| > 4\sqrt{\Lambda_x(\omega)^2 + \Lambda_z(\omega)^2}. \end{cases} \tag{19}$$

The validity of these assumptions will be verified in section 4.3. The spatial approach based on Eq. (1) and Eq. (19) will be used in comparison to the sub-area decomposition technique presented in the following.

3.2 Sub-area decomposition technique with uncorrelated sub-areas

The wavenumber formulation consists in applying the space Fourier-transform to the WPF cross-spectrum defined on a given area, thus for the whole plate in the case of a homogeneous TBL (see section 2.2). Hence, the plate surface is divided into N sub-areas along the streamwise direction. For each of these sub-areas, the TBL is assumed homogeneous, as represented in Fig. 4 in the case of 3 sub-areas. Constant TBL parameters are then attributed to each sub-area, equal to their mean value observed for the sub-area concerned. For each sub-area Σ_ζ, $1 \leqslant \zeta \leqslant N$, the cross-spectrum of the WPF is defined by:

$$\Gamma_{pp}(\tilde{\mathbf{x}}, \tilde{\tilde{\mathbf{x}}}, \omega) = \Psi_{pp,\zeta}(\tilde{\tilde{\mathbf{x}}} - \tilde{\mathbf{x}}, \omega), \text{ if } (\tilde{\mathbf{x}}, \tilde{\tilde{\mathbf{x}}}) \in (\Sigma_\zeta \times \Sigma_\zeta)\,, \tag{20}$$

where $\Psi_{pp,\zeta}$ is the cross-spectrum of the WPF considering the constant TBL parameters attributed to Σ_ζ.

For the sake of simplification, let us suppose that the surface Σ is divided into 2 sub-areas Σ_1 and Σ_2, so that $\Sigma_1 \cup \Sigma_2 = \Sigma$ and $\Sigma_1 \cap \Sigma_2 = \varnothing$. Introducing the sub-area decomposition into Eq. (3) gives:

$$\begin{aligned} S_{vv}(\mathbf{M},\omega) = &\iint_{\Sigma_1}\iint_{\Sigma_1} \mathcal{H}(\mathbf{M},\tilde{\mathbf{x}},\tilde{\tilde{\mathbf{x}}},\omega)\mathrm{d}\tilde{\mathbf{x}}\mathrm{d}\tilde{\tilde{\mathbf{x}}} \\ &+ \iint_{\Sigma_1}\iint_{\Sigma_2} \mathcal{H}(\mathbf{M},\tilde{\mathbf{x}},\tilde{\tilde{\mathbf{x}}},\omega)\mathrm{d}\tilde{\mathbf{x}}\mathrm{d}\tilde{\tilde{\mathbf{x}}} \\ &+ \iint_{\Sigma_2}\iint_{\Sigma_1} \mathcal{H}(\mathbf{M},\tilde{\mathbf{x}},\tilde{\tilde{\mathbf{x}}},\omega)\mathrm{d}\tilde{\mathbf{x}}\mathrm{d}\tilde{\tilde{\mathbf{x}}} \\ &+ \iint_{\Sigma_2}\iint_{\Sigma_2} \mathcal{H}(\mathbf{M},\tilde{\mathbf{x}},\tilde{\tilde{\mathbf{x}}},\omega)\mathrm{d}\tilde{\mathbf{x}}\mathrm{d}\tilde{\tilde{\mathbf{x}}}, \end{aligned} \tag{21}$$

where:

$$\mathcal{H}(\mathbf{M},\tilde{\mathbf{x}},\tilde{\tilde{\mathbf{x}}},\omega) = H_v(\mathbf{M},\tilde{\mathbf{x}},\omega)\Gamma_{pp}(\tilde{\mathbf{x}},\tilde{\tilde{\mathbf{x}}},\omega)H_v^*(\mathbf{M},\tilde{\tilde{\mathbf{x}}},\omega). \tag{22}$$

The second line of the right term of Eq. (21) contains the cross-spectrum $\Gamma(\tilde{\mathbf{x}},\tilde{\tilde{\mathbf{x}}},\omega)$ with $\tilde{\mathbf{x}} \in \Sigma_2$ and $\tilde{\tilde{\mathbf{x}}} \in \Sigma_1$. As seen in section 3.1, the cross-spectrum is a decreasing function of space that is negligible as soon as the distance between the two points is greater than four times the coherence length. Consequently, for $\tilde{\mathbf{x}}$ and $\tilde{\tilde{\mathbf{x}}}$ situated in different sub-areas, it is assumed that their separation is large enough for the corresponding cross-spectrum to be considered as null:

$$\forall(\tilde{\mathbf{x}},\tilde{\tilde{\mathbf{x}}}) \in (\Sigma_2 \times \Sigma_1),\ \Gamma_{pp}(\tilde{\mathbf{x}},\tilde{\tilde{\mathbf{x}}},\omega) = 0. \tag{23}$$

Obviously, this is not strictly true for two points close to a common sub-area edge.

This is equivalent to say that excitation on two sub-areas is decorrelated. The same assumption is applied for the third term of Eq. (21), which becomes:

$$\begin{aligned} S_{vv}(\mathbf{M},\omega) = &\iint_{\Sigma_1}\iint_{\Sigma_1} H_v(\mathbf{M},\tilde{\mathbf{x}},\omega)\Psi_{pp,1}(\tilde{\tilde{\mathbf{x}}}-\tilde{\mathbf{x}},\omega)H_v^*(\mathbf{M},\tilde{\tilde{\mathbf{x}}},\omega)\mathrm{d}\tilde{\mathbf{x}}\mathrm{d}\tilde{\tilde{\mathbf{x}}} \\ &+ \iint_{\Sigma_2}\iint_{\Sigma_2} H_v(\mathbf{M},\tilde{\mathbf{x}},\omega)\Psi_{pp,2}(\tilde{\tilde{\mathbf{x}}}-\tilde{\mathbf{x}},\omega)H_v^*(\mathbf{M},\tilde{\tilde{\mathbf{x}}},\omega)\mathrm{d}\tilde{\mathbf{x}}\mathrm{d}\tilde{\tilde{\mathbf{x}}}. \end{aligned} \tag{24}$$

With the same method applied for an arbitrary number N of sub-areas and assuming the sub-area excitation is decorrelated, Eq. (24) is generalized as follows:

$$S_{vv}(\mathbf{M},\omega) = \sum_{\zeta=1}^{N} \iint_{\Sigma_\zeta}\iint_{\Sigma_\zeta} H_v(\mathbf{M},\tilde{\mathbf{x}},\omega)\Psi_{pp,\zeta}(\tilde{\tilde{\mathbf{x}}}-\tilde{\mathbf{x}},\omega)H_v^*(\mathbf{M},\tilde{\tilde{\mathbf{x}}},\omega)\mathrm{d}\tilde{\mathbf{x}}\mathrm{d}\tilde{\tilde{\mathbf{x}}}. \tag{25}$$

Replacing $\Psi_{pp,\zeta}(\tilde{\tilde{\mathbf{x}}}-\tilde{\mathbf{x}},\omega)$ by its Fourier transform $\Phi_{pp,\zeta}(\mathbf{k},\omega)$, Eq. (25) becomes:

$$S_{vv}(\mathbf{M},\omega) = \frac{1}{4\pi^2}\sum_{\zeta=1}^{N} \iint_{\infty} \left|\hat{H}_{v,\zeta}(\mathbf{M},\mathbf{k},\omega)\right|^2 \Phi_{pp,\zeta}(\mathbf{k},\omega)\mathrm{d}\mathbf{k}, \tag{26}$$

where

$$\hat{H}_{v,\zeta}(\mathbf{M},\mathbf{k},\omega) = \iint_{\Sigma_\zeta} H_v(\mathbf{M},\tilde{\mathbf{x}},\omega)e^{i\mathbf{k}\cdot\tilde{\mathbf{x}}}\mathrm{d}\tilde{\mathbf{x}}. \tag{27}$$

The latter quantity can be interpreted as the plate response in velocity at $\mathbf{M}$ when the surface Σ_ζ is excited by a wall plane wave of wavevector $\mathbf{k}$. In the following, this will be referred to as the sub-area sensitivity function. It can be estimated with an expression similar to Eq. (16):

$$\hat{H}_{v,\zeta}(\mathbf{M}, k_x, k_z, \omega) = \sum_{m,n}^{\infty} \frac{i\omega W_{mn}(\mathbf{M}) \hat{W}_{mn}^{\Sigma_\zeta}(k_x, k_z)}{M_{mn}(\omega_{mn}^2 + i\eta\omega_{mn}\omega - \omega^2)}, \tag{28}$$

where:

$$\hat{W}_{mn}^{\Sigma_\zeta}(k_x, k_z) = \int_0^{L_z} \int_{X_\zeta^0}^{X_\zeta^1} W_{mn}(x, z) e^{i(xk_x + zk_z)} \mathrm{d}x\mathrm{d}z, \tag{29}$$

with X_ζ^0 and X_ζ^1 the x coordinates of the two edges of the sub-area Σ_ζ in ascending order $X_\zeta^0 < X_\zeta^1$. Here, the plate surface Σ is divided only in the stream direction, as illustrated in Fig. 4, because the considered TBL is invariant in the $\vec{z}$ direction.

Two assumptions have been made in this section: the first is that sub-area excitation is decorrelated, which means that coherent turbulent structures located on the borderline between two sub-areas are omitted from the calculation. Then, ideally, the number of sub-areas should be as low as possible. The second assumption is that the TBL can be correctly described by a model with discrete parameters. Hence, the number of sub-areas needs to be chosen to approach the continuous evolution of the TBL parameters. The optimum sub-area discretization will be addressed in section 4.4.

3.3 Sub-area decomposition technique with corrective term

The assumption made previously that the sub-area excitation is decorrelated may be too strong. In this section, a corrective term for Eq. (26) is introduced, in order to take into account interactions between the neighboring sub-areas. This added term is expected to improve the accuracy of the prediction, with a weak additional assumption on the variation of the TBL between two sub-areas. Indeed, it is supposed that the cross-spectrum of the WPF between two points located on two adjoining sub-areas can be approximated by considering the arithmetic mean of the TBL parameters specific to the two sub-areas. If the TBL varies moderately between the two sub-areas, this assumption may certainly be valid and allow us to take interactions between adjoining sub-areas. The cross-spectrum of the WPF between two points belonging to two neighboring sub-areas can be written:

$$\Gamma_{pp}(\tilde{\mathbf{x}}, \tilde{\tilde{\mathbf{x}}}, \omega) \approx \Psi_{pp,\zeta\cup(\zeta+1)}(\tilde{\tilde{\mathbf{x}}} - \tilde{\mathbf{x}}, \omega),\ (\tilde{\mathbf{x}}, \tilde{\tilde{\mathbf{x}}}) \in (\Sigma_\zeta \times \Sigma_{\zeta+1}), \tag{30}$$

where:

- ζ and $\zeta + 1$ are the sub-area indices of two neighboring areas ($1 \leqslant \zeta \leqslant N - 1$);
- $\Psi_{pp,\zeta\cup(\zeta+1)}$ is the cross-spectrum of WPF evaluated with the arithmetic mean of the TBL parameters of the two sub-areas Σ_ζ and $\Sigma_{\zeta+1}$.

Using $\Gamma_{pp}(\tilde{\mathbf{x}}, \tilde{\tilde{\mathbf{x}}}, \omega) = \Gamma_{pp}^*(\tilde{\tilde{\mathbf{x}}}, \tilde{\mathbf{x}}, \omega)$, the sum of the second and third lines of Eq. (21) is:

$$\iint_{\Sigma_1} \iint_{\Sigma_2} \mathcal{H}(\mathbf{M}, \tilde{\mathbf{x}}, \tilde{\tilde{\mathbf{x}}}, \omega) \mathrm{d}\tilde{\mathbf{x}}\mathrm{d}\tilde{\tilde{\mathbf{x}}} + \iint_{\Sigma_2} \iint_{\Sigma_1} \mathcal{H}(\mathbf{M}, \tilde{\mathbf{x}}, \tilde{\tilde{\mathbf{x}}}, \omega) \mathrm{d}\tilde{\mathbf{x}}\mathrm{d}\tilde{\tilde{\mathbf{x}}} = 2\Re\left[\iint_{\Sigma_1} \iint_{\Sigma_2} \mathcal{H}(\mathbf{M}, \tilde{\mathbf{x}}, \tilde{\tilde{\mathbf{x}}}, \omega) \mathrm{d}\tilde{\mathbf{x}}\mathrm{d}\tilde{\tilde{\mathbf{x}}} \right]. \tag{31}$$

Considering Eq. (30), this term can be rewritten:

$$\begin{aligned}
&2\Re\left[\iint_{\Sigma_1}\iint_{\Sigma_2} H_v(\mathbf{M},\tilde{\mathbf{x}},\omega)\Psi_{pp,1\cup2}(\tilde{\tilde{\mathbf{x}}}-\tilde{\mathbf{x}},\omega)H_v^*(\mathbf{M},\tilde{\tilde{\mathbf{x}}},\omega)\mathrm{d}\tilde{\mathbf{x}}\mathrm{d}\tilde{\tilde{\mathbf{x}}}\right]\\
=&2\Re\left[\frac{1}{(2\pi)^2}\iint_{\Sigma_1}\iint_{\Sigma_2}\iint_{\infty} H_v(\mathbf{M},\tilde{\mathbf{x}},\omega)\Phi_{pp,1\cup2}(\mathbf{k},\omega)e^{-i\mathbf{k}\cdot(\tilde{\tilde{\mathbf{x}}}-\tilde{\mathbf{x}})}H_v^*(\mathbf{M},\tilde{\tilde{\mathbf{x}}},\omega)\mathrm{d}\mathbf{k}\mathrm{d}\tilde{\mathbf{x}}\mathrm{d}\tilde{\tilde{\mathbf{x}}}\right] \qquad (32)\\
=&\frac{1}{(2\pi)^2}\,2\Re\left[\iint_{\infty}\hat{H}_{v,1}(\mathbf{M},\mathbf{k},\omega)\Phi_{pp,1\cup2}(\mathbf{k},\omega)\hat{H}_{v,2}^*(\mathbf{M},\mathbf{k},\omega)\mathrm{d}\mathbf{k}\right],
\end{aligned}$$

where $\Phi_{pp,1\cup2}(\mathbf{k},\omega)$ is the spatial Fourier transform of $\Psi_{pp,1\cup2}$.

From Eq. (21) it leads to:

$$\begin{aligned}
S_{vv}(\mathbf{M},\omega) = \frac{1}{(2\pi)^2}\iint_{\infty}\Big(&\left|\hat{H}_{v,1}(\mathbf{M},\mathbf{k},\omega)\right|^2\Phi_{pp,1}(\mathbf{k},\omega)+\left|\hat{H}_{v,2}(\mathbf{M},\mathbf{k},\omega)\right|^2\Phi_{pp,2}(\mathbf{k},\omega)\;\mathrm{d}\mathbf{k}\\
&\ldots+\iint_{\infty}2\Re\left[\hat{H}_{v,1}(\mathbf{M},\mathbf{k},\omega)\Phi_{pp,1\cup2}(\mathbf{k},\omega)\hat{H}_{v,2}^*(\mathbf{M},\mathbf{k},\omega)\right]\Big)\,\mathrm{d}\mathbf{k}. \qquad (33)
\end{aligned}$$

The process can be extended to an arbitrary number N of sub-areas ($N \geqslant 2$) taking only the interactions between neighboring sub-areas into account. By truncating the wavenumber domain to cutoff wavenumbers $(\bar{k}_x,\bar{k}_z)$, the expression is therefore:

$$\begin{aligned}
S_{vv}(\mathbf{M},\omega) = \frac{1}{4\pi^2}\sum_{\mathbf{k}\in\Omega_{\mathbf{k}}}\Bigg(&\sum_{\zeta=1}^{N}\left|\hat{H}_{v,\zeta}(\mathbf{M},\mathbf{k},\omega)\right|^2\Phi_{pp,\zeta}(\mathbf{k},\omega)\\
&\ldots+\sum_{\zeta=1}^{N-1}2\Re\left[\hat{H}_{v,\zeta}(\mathbf{M},\mathbf{k},\omega)\Phi_{pp,\zeta\cup(\zeta+1)}(\mathbf{k},\omega)\hat{H}_{v,\zeta+1}^*(\mathbf{M},\mathbf{k},\omega)\right]\Bigg)\delta k_x\delta k_z. \qquad (34)
\end{aligned}$$

The second term of Eq. (34) is the corrective interaction term.

4 Numerical application with a homogeneous TBL

4.1 Presentation of the case

Before dealing with the case of non-homogeneous TBL, a homogeneous TBL is considered to fulfill three purposes:

- first, to verify that the contributions of the convective peak of the WPF have a negligible effect on the vibrations of the panel considered;
- second, to verify the assumption made by Eq. (19) for the spatial approach;
- last, to define validity criteria for the assumptions of the sub-area decomposition technique.

Let us consider a flat plate in an air flow and excited by a homogeneous TBL. The plate is made of aluminum. Plate dimensions L_x and L_z, material Young's modulus E, Poisson's ratio ν_p and mass density ρ_p are given in Table 1. The plate thickness is $h = 4\,\mathrm{mm}$. The fluid density ρ and kinematic viscosity ν, TBL external velocity U_e, thickness δ and shear stress τ are given in Table 2. Structural damping η is set at 1% for all modes. Flexural rigidity D, found in Eq. (12) and Eq. (14), is deduced from E and ν_p:

$$D = \frac{Eh^3}{12(1-\nu_p^2)}. \qquad (35)$$

Plate		Material		
L_x	L_z	E	ν_p	ρ_p
1.00 m	0.35 m	68.9 GPa	0.35	2740 kg.m^{-3}

Table 1: Plate dimensions and material characteristics.

Fluid			TBL	
ρ	ν	U_e	δ	τ
1.22 kg.m^{-3}	1.5×10^{-5} m^2.s^{-1}	40 m.s^{-1}	1.0 cm	2.7 Pa

Table 2: Fluid and homogeneous TBL parameters.

The WPF wavenumber-frequency spectrum can be expressed in function of an autospectrum $S_{pp}(\omega)$ and a normalized cross-spectrum $\tilde{\Phi}_{pp}(k_x, k_z, \omega)$ (Graham, 1997):

$$\Phi_{pp}(k_x, k_z, \omega) = S_{pp}(\omega)\tilde{\Phi}_{pp}(k_x, k_z, \omega)k_c^{-2}. \tag{36}$$

For a flat plate with a zero pressure gradient, the Goody model (Goody, 2004) is considered for the autospectrum:

$$S_{pp}(\omega) = \frac{\delta\tau^2}{U_e} \times \frac{c_2(\omega\delta/U_e)^2}{[(\omega\delta/U_e)^{0.75} + c_1]^{3.7} + [c_3 R_T^{-0.57}(\omega\delta/U_e)]^7}, \tag{37}$$

where $R_T = (\delta/U_e)/(\nu/u_\tau^2)$ and the constants are $c_1 = 0.5$, $c_2 = 3$ and $c_3 = 1.1$. For an incompressible flow, the friction velocity $u_\tau = \sqrt{\tau/\rho}$ is calculated with the TBL shear stress τ and the fluid density ρ, whereas for a flat plate, external velocity U_e is equal to free flow speed U_0.

For the normalized cross-spectrum of the WPF, the Mellen elliptical model (Mellen, 1990) has been chosen because of its simple expression and its more realistic prediction in the low wavenumber region than the Corcos model:

$$\tilde{\Phi}_{pp}(k_x, k_z, \omega) = \frac{2\pi\alpha_x^2\alpha_z^2 k_c^3}{\sqrt{(\alpha_x\alpha_z k_c)^2 + (\alpha_x k_z)^2 + \alpha_z^2(k_x - k_c)^2}^3}, \tag{38}$$

where coefficients α_x and α_z are given in section 3.1. For the sake of simplicity, convective speed U_c is assumed to be a constant fraction of the external velocity U_e:

$$U_c = 0.7U_e. \tag{39}$$

4.2 Wavenumber approach: influence of the convective peak

In order to evaluate the influence of the convective peak on the panel response, two calculations using the wavenumber method are achieved. The first one uses the cutoff wavenumbers μk_f defined by Eq. (9) with $\mu = 1.2$. For the second one, cutoff wavenumbers $\bar{k}_x$ and $\bar{k}_z$ have both been set to 160 rad/m, which is equal to 1.2 times the convective wavenumber k_c at 600 Hz. In the first scenario, the cutoff wavenumber is smaller than the convective wavenumber on the frequency range considered, so this calculation neglects the influence of the convective peak. On the contrary, the second calculation includes the effect of the convective peak of the WPF.

The results of the two calculations are shown in Fig. 5, in terms of the spatial mean of the velocity autospectrum (SMVA) on the plate. Since the first resonance of the studied plate occurs at $f_{11} = 89$ Hz, the lower bound of the frequency band of interest has been set at 80 Hz. Good agreement can be observed between predictions both with and without the convective peak. The main discrepancy is located in the lower frequencies, where the convective peak slightly influences the vibrational response. This difference is below 0.5 dB above 300 Hz confirming that the convective components of the WPF make negligible contributions to the panel vibrations for frequencies well above f_{aero}.

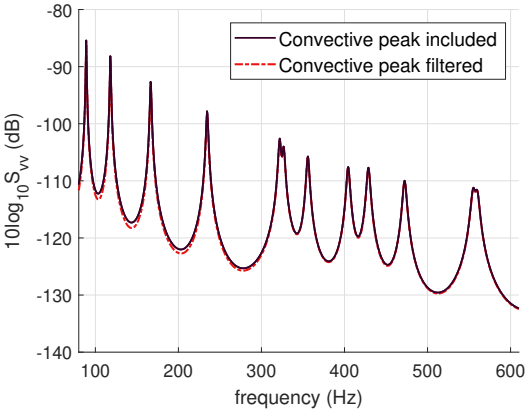

Figure 5: Level of the spatial mean velocity autospectrum of the panel excited by a homogeneous turbulent boundary layer. Comparison of two wavenumber calculations, including the convective peak or not (dB, ref. 1 (m/s) ^ 2/Hz).

4.3 Spatial approach: validation of the assumption of weak spatial correlation

In section 3.1, it has been stated that since the WPF of a TBL is weakly correlated spatially, the cross-spectrum of the WPF can be negligible when the separation between the two points is significant relatively to the coherence length. In Fig. 6, the SMVA is plotted considering a spatial calculation and a homogeneous TBL. Two cases are compared: Eq. (4) with Eq. (2) considers the cross-correlation of the WPF between all the couples of grid points of the spatial mesh, whereas the second one considers the assumptions made in Eq. (19) (that is to say that the cross correlations of the WPF are neglected when the separation between two grid points is greater than four times the coherence length).

Good agreement between the two spatial calculations can be observed in Fig. 6. The conclusion drawn here is that when two points are distant enough, their correlation plays a negligible role in the vibrational response, and Eq. (19) is a good approximation.

4.4 Definition of a criterion on the sub-area length

The sub-area decomposition technique was introduced in sections 3.2 and 3.3. For both approaches, interactions between neighboring sub-areas have been either neglected or approximated. A minimum number of sub-areas is necessary to have an accurate description of TBL evolution. However, increasing the number of sub-areas may increase the error, because of the approximations made on the TBL spatial correlation at the borderlines of the sub-areas. In this section, a criterion applied to the size of the sub-areas to minimize errors while preserving an optimal description of the TBL variations is suggested. This criterion will be established on the basis of numerical comparisons on the panel test case considering a homogeneous excitation. The assumptions concerning the interactions between sub-areas occur either for a homogeneous TBL and for a non-homogeneous one. However, we can easily obtain a reference result for the former that can be compared to the SDT results with different numbers of sub-areas, as illustrated in Fig. 7. Indeed, the discrepancy between the results considering one area and those considering N sub-areas corresponds to the error introduced by neglecting certain sub-area interactions.

Two SDT calculations are performed: the first one leaving out the interactions between the sub-areas, as described in section 3.2, and the second one considering the interactions between the neighboring sub-areas, as described in section 3.3. Fig. 8 shows the absolute difference of the SMVA between the SDT with $N = 1$

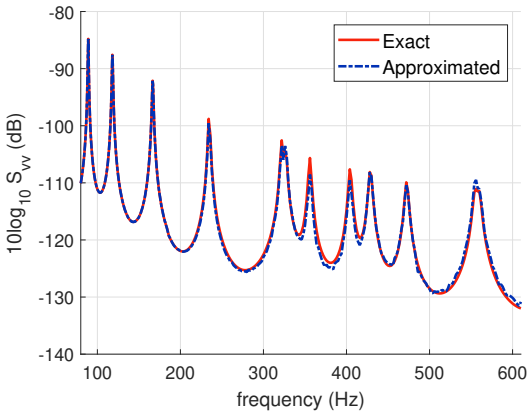

Figure 6: Level of spatial mean of the velocity autospectrum under a homogeneous TBL. Comparison of: exact spatial, considering all grid point couples, and approximated spatial, with the assumption of Eq. (19) (dB, ref. 1 (m/s) ^ 2/Hz).

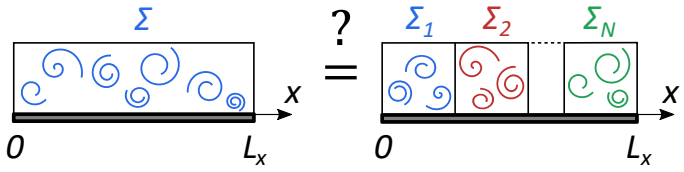

Figure 7: Illustration of the SDT application for a homogeneous TBL.

and with $N = 8$. As expected, the difference is always greater without the interactions, except below 100 Hz. Above 150 Hz, the absolute difference is never higher than 0.4 dB with the interaction term whereas it reaches 2.4 dB without taking it into account. This highlights the benefit of corrective terms in the SDT. Moreover, the maxima of the error are observed at the resonant frequencies (symbolized by squares on Fig. 8). In the following, the errors will be estimated at these resonant frequencies only.

4.5 Methodology for extracting the criteria

Previously, it was shown that the convective peak of the WPF has a negligible effect on the plate vibrations because flexible structures are mainly sensitive to the sub-convective part of the WPF spectrum for frequencies well above the aerodynamic coincidence frequency. The result is that the wavenumber calculations related to the SDT can be truncated to cutoff wavenumbers defined by Eq. (9). The truncated spectrum of the TBL WPF is relatively flat and can be roughly represented by a white-noise spectrum, as illustrated in red in Fig. 2. In the first step, the panel will be excited by a homogeneous random excitation with a low-wavenumber white noise spectrum. Considering this academic excitation instead of the TBL excitation permits studying the influence of the cutoff wavenumbers independently of the presence of the convective peak of a TBL excitation. In others words, calculations with different values of cutoff wavenumber of the white noise spectrum can be carried out without specific precautions compared to the convective wavenumber.

The Fourier transform of a gate function, that gives the spatial cross-spectrum of the WPF, is a cardinal sinus function:

$$\Gamma_{pp}(x,z,\omega) = \frac{1}{(2\pi)^2}\int_{-\bar{k}_x}^{\bar{k}_x}\int_{-\bar{k}_z}^{\bar{k}_z} e^{-j(xk_x+zk_z)}\mathrm{d}k_x\mathrm{d}k_z = \frac{\bar{k}_x\bar{k}_z}{\pi^2}\,\mathrm{sinc}\left(\bar{k}_x x\right)\mathrm{sinc}\left(\bar{k}_z z\right). \tag{40}$$

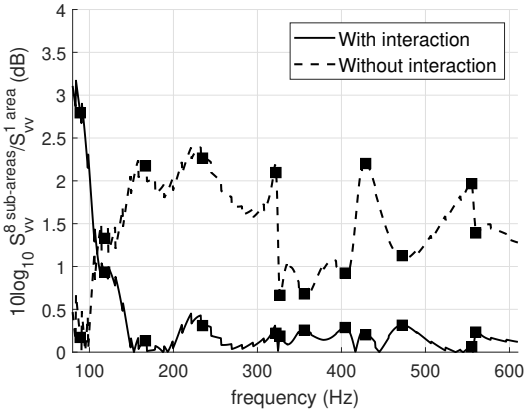

Figure 8: Difference of the spatial mean of the velocity autospectrum between the calculations considering 8 sub-areas and 1 area (squares indicate modal frequencies).

The spatial coherence of the form $\mathrm{sinc}(\bar{k}_x x)$ corresponds to the one of a diffuse field (Cook et al., 1955) when $\bar{k}_x = k_0$, the acoustic wavenumber. However, in the present case, $\bar{k}_x$ can be chosen independently of the acoustic wavenumber for the purpose of the study.

The higher $\bar{k}_x$ is, the lower the half period of the cardinal sinus function, thus the lower the coherence length of the pressure field in the stream direction. The influence of the spatial correlation of the WPF on the accuracy of the SDT will be studied through the variations of $\bar{k}_x$. It is expected that the lower the coherence length of the WPF, the higher the number of the sub-areas that can be considered in the SDT will be. In the following, the discrepancies of SMVA between the reference calculation and the SDT calculations will be observed.

Let us consider sub-areas of the same size. For N sub-areas, their length is L_x/N. This sub-area length is compared to the coherence length of the white spectrum $2\pi/\bar{k}_x$, in order to extract a criterion for the cases with and without interactions between neighboring sub-areas.

These criteria will first be defined for the white noise excitation in the section 4.6 and their validity will the be verified in section 4.7.

4.6 Spatial white-noise excitation

The rectangular plate, whose thickness and material are described by the parameters given in Table 1, is excited by a spatially homogeneous random excitation having a white noise cross-spectrum in the wavenumber domain. The amplitude of the spectrum is set to a unit value, whereas the cutoff wavenumber in the streamwise direction is defined by $\bar{k}_x = \mu k_f$. Changing the value of μ will change the value of $\bar{k}_x$.

SDT calculations were carried out for a number of sub-areas N ranging from 2 to 12. These quantities are plotted on 3 figures as a function of the ratio of the sub-area length in the streamwise direction over the coherence length associated with the white-noise excitation. Every dot on the graphs represents the difference of mean velocity at a modal frequency between a calculation considering $N \in \{2, ..., 12\}$ sub-areas and another one considering only one area. The results have been plotted for different values of μ and different plate sizes:

- $L_x = 1.0\,\mathrm{m}$, $L_z = 0.35\,\mathrm{m}$ (initial plate dimensions) on Fig. 9;
- $L_x = 0.5\,\mathrm{m}$, $L_z = 0.35\,\mathrm{m}$ on Fig. 10;

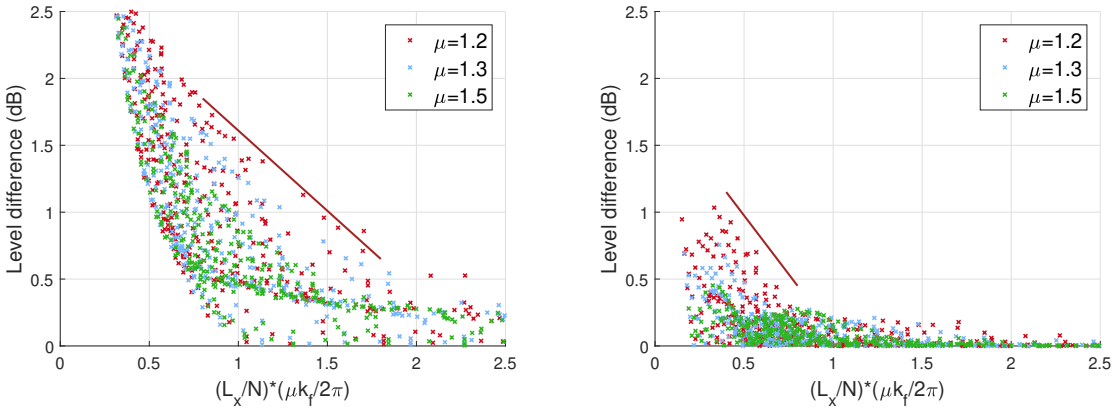

Figure 9: Differences of spatial mean of velocity autospectrum at resonant frequencies between the SDT calculation considering $N \in [2; 12]$ and the reference calculation $N = 1$; $L_x = 1\,\text{m}$, $L_z = 0.35\,\text{m}$; (a), without interaction; (b), with interaction.

- $L_x = 1.0\,\text{m}$, $L_z = 0.20\,\text{m}$ on Fig. 11.

A general trend on all the figures can be observed: the discrepancies decrease globally when the sub-area length increases. Moreover, as expected, the discrepancies are smaller when the interactions with the neighboring sub-areas are taken into account. This leads us to define two criteria: one for each type of calculation.

For both with and without interactions, a linear curve has been drawn as a full line on the different figures corresponding to plates of different sizes. They constitute envelopes for the different data whatever the plate considered. Therefore, criteria can be deduced from these curves and reasonably extrapolated to rectangular plates with a wide variety of dimensions. Considering that an error lower that 1 dB is acceptable in practice, the criterion for the SDT without interaction terms is set to:

$$\frac{L_x}{N} > \frac{3}{2}.\frac{2\pi}{\bar{k}_x}, \tag{41}$$

whereas that for the STD with the interaction terms is set to:

$$\frac{L_x}{N} > \frac{1}{2}.\frac{2\pi}{\bar{k}_x}, \tag{42}$$

where $2\pi/\bar{k}_x = \lambda_f/\mu$.

4.7 TBL excitation

Eq. (41) and Eq. (42) have been defined considering plates excited by a random excitation with a white noise spectrum. Now, their validity will be verified for plates excited by a TBL excitation when the convective components of the WPF can be neglected, as discussed in section 4.2. To do this, the Mellen model is considered with different values of μ to filter the low wavenumber components of the WPF using Eq. (9). The results are plotted in Fig. 12 for the plate and flow characteristics presented in Table 1 and Table 2 respectively. The envelopes defined in the previous section is also carried over on this figure for comparison. They remain globally valid for the TBL excitation. However, some points are above these curves, especially for the higher values of μ and when the interaction with the neighboring sub-areas are not taken into account.

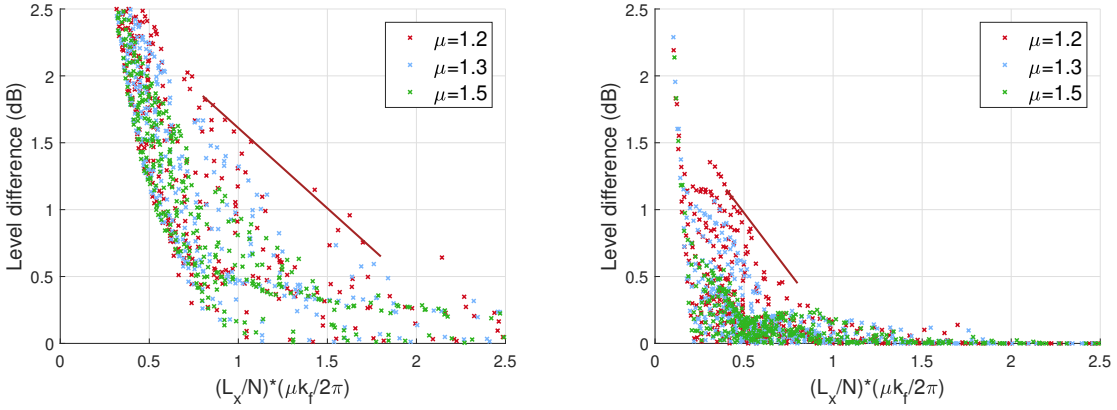

(a) (b)

Figure 10: Same type of results than Fig. 9;
$L_x = 0.5\,\mathrm{m}$, $L_z = 0.35\,\mathrm{m}$; (a), without interaction; (b), with interaction.

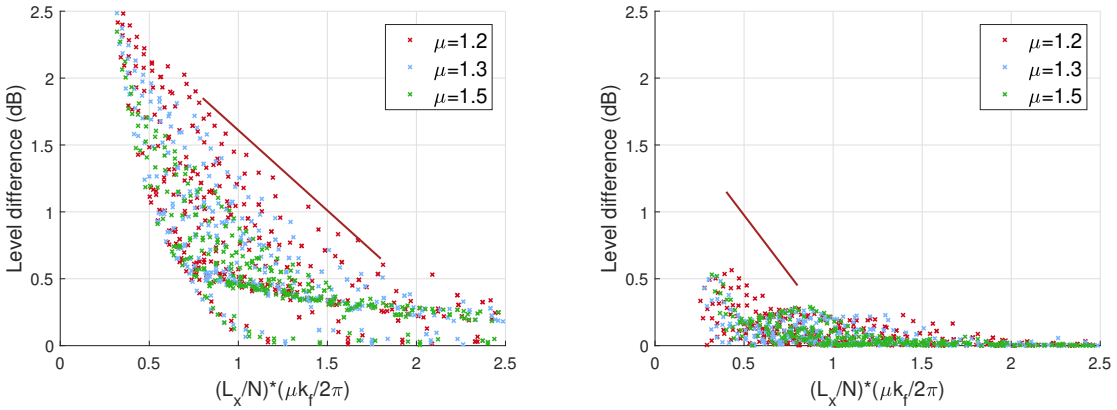

(a) (b)

Figure 11: Same type of results than Fig. 9;
$L_x = 1\,\mathrm{m}$, $L_z = 0.20\,\mathrm{m}$; (a), without interaction; (b), with interaction.

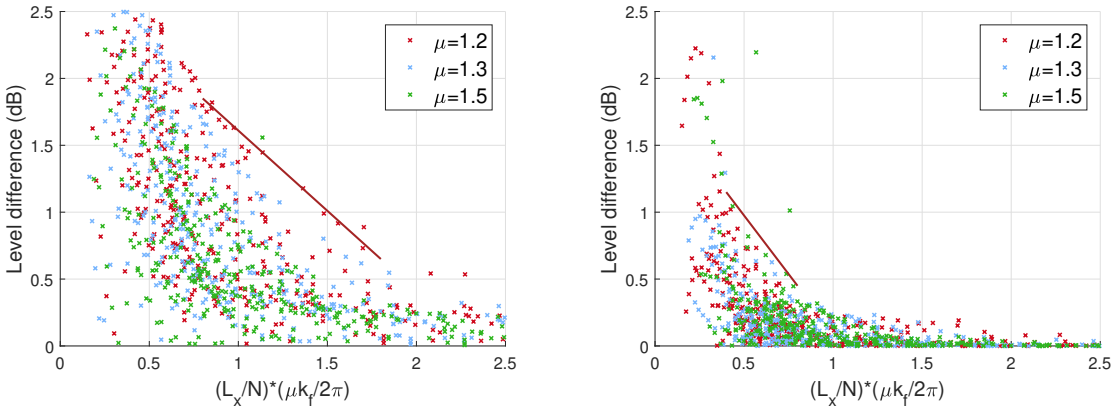

Figure 12: Same simulations as in Fig. 9 with a TBL excitation (Mellen model); $L_x = 1\,\text{m}$, $L_z = 0.35\,\text{m}$; (a) without interaction; (b) with interaction.

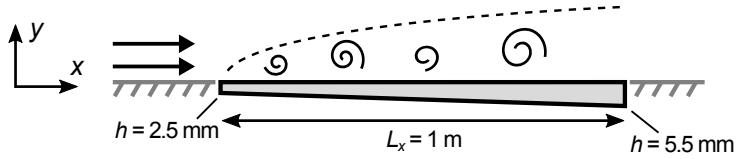

Figure 13: 2-D view of the baffled plate excited by a one-sided flow.

This can be explained by the fact that in the lower part of the frequency range, some components of the convective peak are taken into account when considering the highest values of μ. This shows that the criteria proposed are suitable when the convective components of the WPF can be neglected.

5 Illustration of application for a non-homogeneous TBL

The sub-area decomposition technique is now applied and numerically verified for a non-homogeneous TBL. The considered test case is composed of a thin rectangular plate mounted in an infinitely rigid baffle and an air flow on one side of the plate in the $\vec{x}$ direction. The TBL is supposed to start at the plate leading edge $x = 0$, then grow until the trailing edge $x = L_x$, leading to a non-homogeneous loading of the vibrating plate. To accentuate the effect of the non-homogeneous excitation on the plate vibrations, the thickness of the plate h varies linearly between its leading edge and its trailing edge. The plate is assumed to be simply supported on its four edges and to be made of aluminum (see mechanical parameters in Table 1). A 2-D view of the plate mounted in the baffle and excited by the growing TBL is shown in Fig. 13. The figure is not at scale. It is assumed that the weak slope of the plate surface has no effect on the flow. The model of TBL over a flat plate is therefore preserved (with $U_e = U_0$).

5.1 The plate model

The normal modes of the plate are now extracted from a finite element calculation using the MSC Nastran software. A mesh composed of 160 × 56 nodes and 8745 quadrilateral linear elements (CQUAD4) is considered. This gives around 30 elements per flexural wavelength and 7 elements per convective wavelength at 600 Hz, while the usual criterion is 4 elements per flexural wavelength.

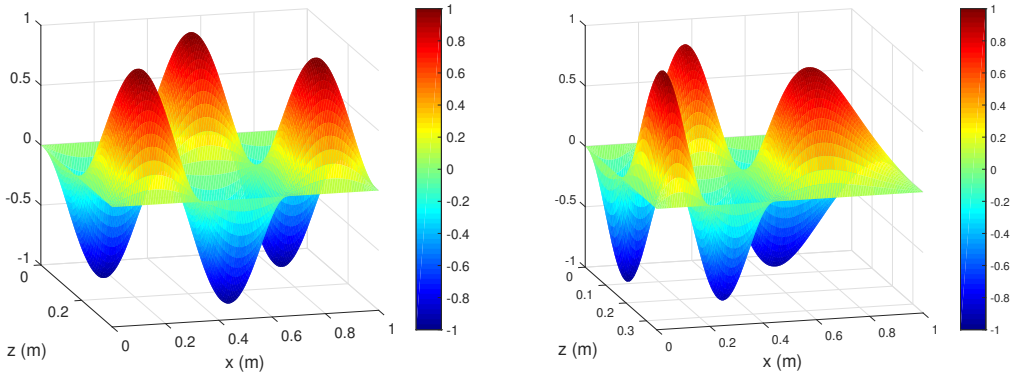

Figure 14: 8^{th} mode shape; (a) constant thickness 403 Hz; (b) non-constant thickness 404 Hz.

Shell properties (PSHELL) are attributed to the elements and the thickness is given at the four nodes of each quadrilateral element. Isotropic material properties (MAT1) are defined using the characteristics from Table 1. The plate modes are extracted with a normal modal analysis (SOL103).

To illustrate the effects of non-constant thickness, the modal shape of the 8^{th} mode is shown in Fig. 14 for the test plate and for an equivalent plate with a constant thickness of 4 mm. For the latter plate, the mode follows the sinusoidal shape of Eq. (11), with a constant distance between the nodal line (i.e. 0.33 m in the $\vec{x}$ direction). Conversely, for the former one, the distance between the nodal line along the $\vec{x}$ direction changes from 0.20 m for the thinner part of the plate to 0.46 m for the thicker part.

To perform the calculation with the SDT, the modal frequencies and the modal shapes are imported in MATLAB. Fast Fourier transforms are used for expressing the mode shapes in the wavenumber domain that intervenes in the calculation of the sub-area sensitivity functions with Eq. (28) and Eq. (29).

Moreover, the cutoff wavenumber in the streamwise direction $\bar{k}_x$ used to filter the convective peak is defined as $\bar{k}_x = \mu k_f^{2.5\text{mm}}$, where $k_f^{2.5\text{mm}}$ is the flexural wavenumber of a flat plate with a constant thickness equal to the minimum thickness of the test plate, that is to say 2.5 mm. As the flexural wavenumber considered is related to the thinner part of the panel, the criterion on the cutoff wavenumber includes the dynamic behavior of the other part of the panel. In the following, μ is set to 1.3.

5.2 Analytical model of a turbulent boundary layer over a flat plate

The plate is inserted in a baffle and excited by a TBL starting at $x = 0$ where the $\vec{x}$ axis corresponds to the streamwise direction. By neglecting static pressure gradients and laminar/transitional areas of the TBL, the parameters of the TBL induced by the constant flow can be estimated with an analytical model from Sanders (2014), where TBL thickness δ and shear stress τ are functions of the local Reynolds number $Re_x = U_0 x/\nu$:

$$\begin{aligned} \delta &= \frac{0.37x}{Re_x^{1/5}}\,, \\ \tau &= \frac{1}{2}\rho U_0^2 \frac{0.0592}{Re_x^{1/5}}\,. \end{aligned} \tag{43}$$

Using these equations, the TBL parameters are plotted in Fig. 15 along the $\vec{x}$ direction, for a flow speed $U_0 = 40$ m/s. From these parameters and Eq. (37), Goody autospectrum can be evaluated along the streamwise direction. The result is shown in Fig. 16. The energy of the excitation is concentrated near the

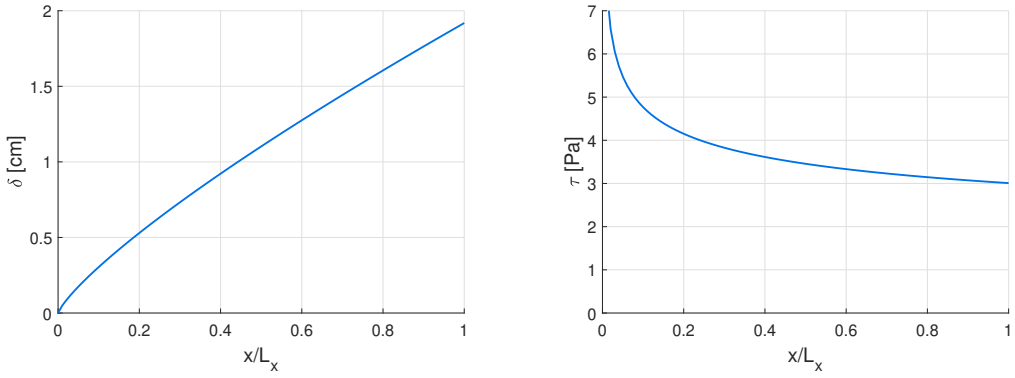

(a) (b)

Figure 15: Analytical model of the flat plate for (a), the TBL thickness δ and (b), the shear stress τ ; $U_0 = 40\,\mathrm{m/s}$.

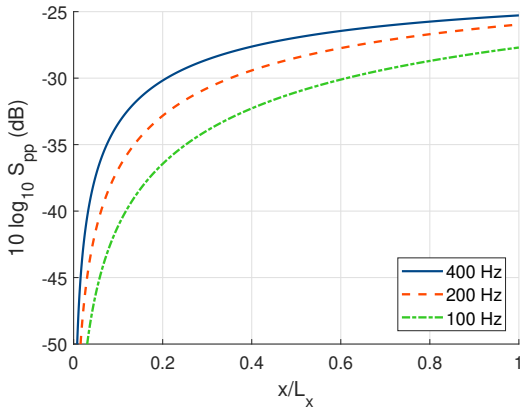

Figure 16: Goody autospectrum resulting from Eq. (43) and Eq. (37); $U_0 = 40\,\mathrm{m/s}$.

trailing edge of the plate, which corresponds to the area where the boundary layer thickness is the highest, as shown in Fig. 15(a). Moreover, the variations of the autospectrum along the $\vec{x}$ direction depend on the frequency. The spatial approach as well as the SDT are able to take into account these variations through their process described in the sections 3.1 and 3.3, respectively. Let it be noted that for the present case, the TBL parameters and therefore the WPF autospectrum are invariant in the $\vec{z}$ crosswise direction.

5.3 Results

The vibration velocity autospectrum of the plate with a varying thickness is calculated with four methods:

- first, the spatial approach with a homogeneous TBL (i.e. Eq. (4)). The TBL parameters were set to the spatial average of the varying TBL parameters shown in Fig. 15, that is to say $\delta = 1.07\,\mathrm{cm}$ and $\tau = 3.76\,\mathrm{Pa}$;
- second, the wavenumber approach considering the same homogeneous TBL (i.e. with Eq. (8)). Contrary to the spatial approach, this calculation does not take the convective contributions into account;

- third, the spatial approach described in section 3.1, that takes into account the spatial variations of the WPF. It gives us a point of comparison for verifying the validity of SDT and the criterion proposed for this case, and for highlighting the interest of SDT in terms of computing time. Due to this computing time, the frequency step for spatial methods is $\Delta f = 2\,\text{Hz}$;
- fourth, the SDT taking into account the interactions between the neighboring sub-areas as described in section 3.3 (i. e. Eq. (34)). 5 sub-areas were considered, to conform to the criterion of Eq. (42) above the first modal frequency at 83 Hz. With this model, the frequency step is $\Delta f = 0.5\,\text{Hz}$.

The comparison of the results of the spatial and of the wavenumber approaches for the homogeneous TBL allows us to verify the negligible influence of the convective contributions for frequencies above three times the aerodynamic coincidence frequency attributed to the thinner part of the plate, that is to say above 96 Hz (comparison not shown).

The results in terms of the spatial mean of the velocity autospectrum (SMVA) on the plate as a function of the frequency are plotted in Fig. 17. The results of the SDT with 5 sub-areas are compared with the wavenumber approach considering the homogeneous TBL. Some differences can be noticed that highlight the importance of taking the spatial variations of the TBL parameters through the variations of the autospectrum of the WPF and the sub-area decomposition. For instance, at 100 Hz, the autospectrum of the WPF estimated with the mean TBL values over the whole plate surface was $-30.6\,\text{dB}$. This value was taken into account in the wavenumber approach considering the homogeneous TBL, whereas the values for the 5 sub-areas of the SDT were: $-40.8\,\text{dB}$, $-33.9\,\text{dB}$, $-31.1\,\text{dB}$, $-29.3\,\text{dB}$ and $-28.2\,\text{dB}$ from leading to trailing edge. These values are coherent with the autospectrum displayed in Fig. 16.

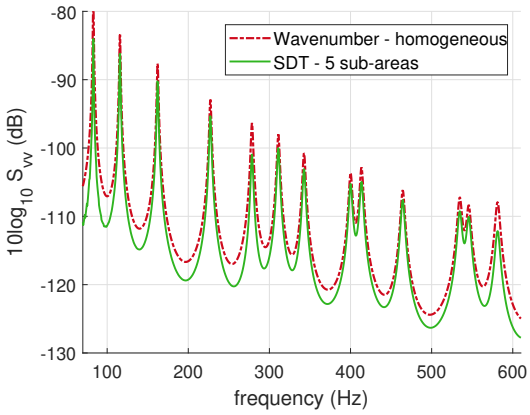

Figure 17: Level of the spatial mean of the velocity autospectrum of the considered test case. Comparison of two calculations: wavenumber approach considering a homogeneous TBL (dashed line), SDT considering the growing TBL through 5 sub-areas with interactions (continuous line) (dB, ref. 1 (m/s) ^ 2/Hz).

In Fig. 18, the difference of the mean plate velocity in dB between a calculation taking the TBL variations into account and another one considering the homogeneous TBL with averaged parameters, separately for the spatial and SDT approaches, is plotted in function of the frequency. Results are colored in gray below 96 Hz, that is to say three times the aerodynamic coincidence frequency (where $k_f^{2.5\text{mm}} = k_c$). The good agreement between the two approaches that can be observed in Fig. 18 permits to validate numerically the ability of the SDT to describe the effect of a growing TBL on the panel vibration.

A difference of globally 2 to 3 dB between the non-homogeneous TBL calculation and homogeneous TBL one occurs, as it can be observed in Fig. 18. Furthermore, two jumps appear, at 279 and 581 Hz with

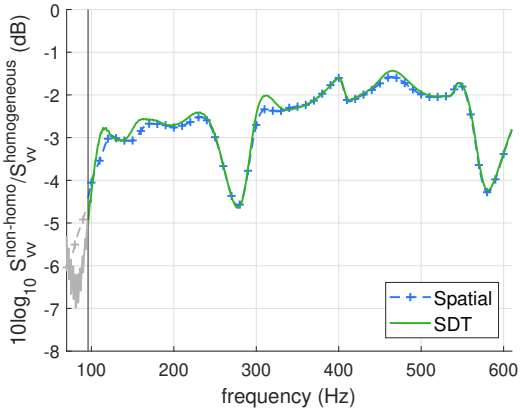

Figure 18: Influence of TBL inhomogeneity: difference between a non-homogeneous TBL calculation and a homogeneous TBL one. Comparison of two types of non-homogeneous TBL calculation: SDT (5 sub-areas, with interactions) and the spatial approach. $U_0 = 40\,\text{m/s}$. Vertical black line: lower frequency limit for SDT (i.e. $3 \times f_{\text{aero}}$).

a difference of 4.6 and 4.2 dB respectively. When looking at the modal frequencies, these two frequencies correspond to the 5^{th} and 13^{th} modes. The modal shapes of these two modes are plotted in Fig. 19. The first half (*i.e.* $0 < x < L_x/2$), where the plate is thinner, is deformed, while the second half (*i.e.* $L_x/2 < x < L_x$), remains undeformed. As highlighted in Fig. 16, the TBL excitation is maximum near the trailing edge (x close to L_x) whereas it is negligible near the leading edge (x close to 0). The exciting pressure fails to excite these modes and so their response is lower compared to the one obtained supposing a homogeneous TBL. For other modes like the one presented in Fig. 14(b), the effect of the non-homogeneity is less important on the panel response than for the 5^{th} and 13^{th} modes because they exhibit deformations on all the plate surface. These results highlights the interest of describing the effect of the spatial variations of the TBL in vibratory calculations.

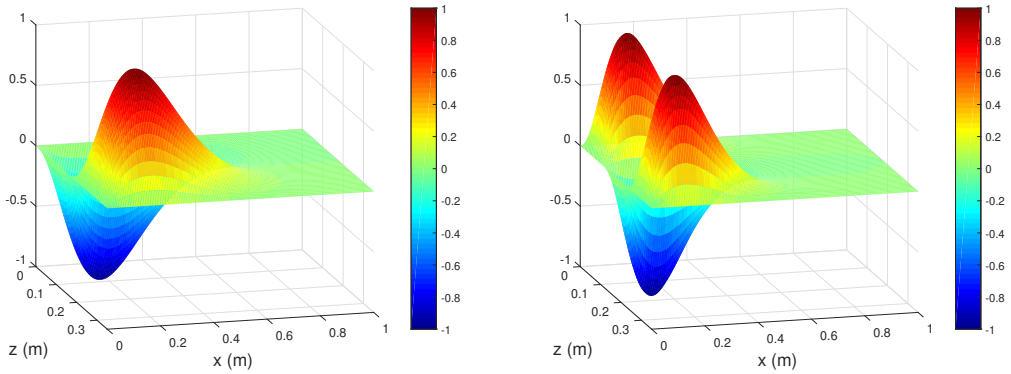

(a) (b)

Figure 19: (a): 5^{th} and (b): 13^{th} modal shapes; 279 Hz and 581 Hz respectively.

The same type of results as Fig. 18 are obtained for two additional velocities: a lower velocity, 20 m/s and a higher one, 60 m/s. The results are shown in Fig. 20. As the same mesh was used for the different flow

speed, the upper frequency of convergence for the spatial approach (based on a criterion on the convective wavelength) depends on the flow speed. For $U_0 = 20\,\mathrm{m/s}$, it is of 350 Hz whereas it is well above 600 Hz for $U_0 = 60\,\mathrm{m/s}$. The results of the spatial approach are then plotted up to 350 Hz in Fig. 20(a). Moreover, the curve of SDT in Fig. 20(b) is colored in gray below 218 Hz, that corresponds to three times the aerodynamic coincidence frequency. A good agreement can be observed between the SDT and the spatial approach for these two supplementary flow speeds. Moreover, higher the flow speed is, higher the difference with the homogeneous TBL calculation is. These increases in the difference with the flow speed is however not uniform in the whole frequency range. For instance, if one focus on the difference at 279 Hz corresponding to the frequency of the 5^{th} mode, the differences are 3.2, 4.6 and 5.8 dB, respectively at 20 m/s, 40 m/s, and 60 m/s, whereas at 350 Hz which does not correspond to a particular mode, the differences are 1.7, 2.3 and 3.0 dB for the same flow speeds. The increase at 279 Hz from 20 m/s to 60 m/s is then 2.6 dB whereas it is only of 1.3 dB at 350 Hz. The proposed SDT is able to describe these variations in accordance with the spatial approach.

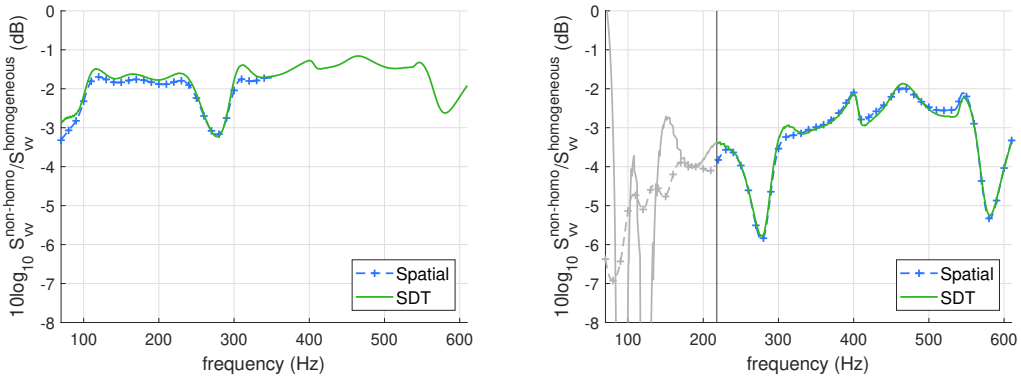

Figure 20: Influence of TBL inhomogeneity: same type of results than Fig. 18 for two different flow speed. (a), $U_0 = 20\,\mathrm{m/s}$; (b), $U_0 = 60\,\mathrm{m/s}$. Vertical black line: lower frequency limit for SDT (i.e. $3 \times f_{\mathrm{aero}}$).

Finally, let us focus on computing time. The calculations were performed on a server computer (Intel Core i7-4930K 3.40 Ghz, 64 Go RAM). The spatial method required around 100 hours of computation whereas the SDT results were obtained in under 30 minutes. This highlights the huge time-benefit of the sub-area decomposition technique compared to the spatial method, especially considering the difference in frequency step (i.e. 2 Hz for the spatial approach compared to 0.5 Hz for the SDT), while the predictions are similar for both approaches for a non-homogeneous excitation.

6 Conclusion

In this paper, we focused on the prediction of the dynamic behavior of panels excited by a non-homogeneous turbulent boundary layer. The investigations started from the two approaches generally used for dealing with homogeneous TBL, namely the spatial and the wavenumber approaches. While the extension of the spatial approach to non-homogeneous excitations was relatively straightforward, the extension of the wavenumber approach required more developments and assumptions that led to the sub-area decomposition technique (SDT). The result was that the latter required much less computation time than the former. Two versions of the SDT were proposed: the first assumed homogeneous TBL excitation on each sub-area and neglected the interaction between the different sub-areas. This latter assumption can be justified at first sight by the

fact that the coherence length of the WPF of the TBL was generally small in comparison to the sub-area sizes considered. However, it was observed numerically that this assumption may be too strong in some situations. To circumvent this issue, the second version took the interactions with the neighboring sub-areas into account. As the two versions of SDT were based on a simplifying assumption concerning the spatial correlation of the WPF, a numerical study was carried out to propose criteria for the minimum sizes of the sub-areas as a function of the minimum wavelength of the WPF. The criterion of Eq. (41) for the SDT version without interaction between sub-areas was naturally more restrictive than that of Eq. (42) for the STD version with interaction with neighboring sub-areas.

The numerical simulations carried out and compared with the spatial approach showed that the SDT is suitable when the convective components of the WPF can be neglected, that is to say for frequencies that are at least three times greater than the aerodynamic coincidence frequency. In this condition and when the criterion of Eq. (41) or Eq. (42) (depending of the SDT version) is respected, the approach proposed gave accurate results.

An application to a rectangular plate with linearly varying thickness under an increasing TBL allowed us to highlight the interest of describing the effect of the spatial variations of the WPF with SDT compared to a prediction assuming a homogeneous TBL. These approaches exhibits a global difference of 2 to 6 dB, depending on the flow speed. In particular, we observed that significant differences (up to 6 dB) could be observed for certain resonant frequencies. These frequencies concerned modes of the plate that were weakly deformable on an area highly excited by the TBL. Only approaches taking into account the spatial variations of the TBL parameters like the spatial method and the SDT are capable of describing such phenomenon. However, the SDT was significantly less demanding in terms of computer resources than the spatial approach, the downside being that the SDT was valid when the convective peak was negligible. It appears that this approach is not dedicated to the aeronautical applications for which the flow speed is high. However, it can be adapted to the automotive applications for which the considered speeds are relatively low as well as to the naval applications characterized by thick structures and low speeds.

Acknowledgments

This work was supported by the French Ministère des Armées, under the responsibility of the Agence de l'Innovation et de la Défense, and performed within the framework of the Labex CeLyA of Université de Lyon, supervised by the French National Research Agency (ANR-10-LABX-0060/ ANR-11-IDEX-0007).

References

Arguillat, B., Ricot, D., Robert, G., Bailly, C., 2005. Measurements of the wavenumber-frequency spectrum of wall pressure fluctuations under turbulent flows, in: 11th AIAA/CEAS Aeroacoustics Conference.

Bonness, W.K., Capone, D.E., Hambric, S.A., 2010. Low-wavenumber turbulent boundary layer wall-pressure measurements from vibration data on a cylinder in pipe flow. Journal of Sound and Vibration 329, 4166–4180.

Caiazzo, A., D'Amico, R., Desmet, W., 2016. A generalized Corcos model for modelling turbulent boundary layer wall pressure fluctuations. Journal of Sound and Vibration 372, 192–210.

Chase, D., 1980. Modeling the wavevector-frequency spectrum of turbulent boundary layer wall pressure. Journal of Sound and Vibration 70, 29–67.

Chase, D., 1987. The character of the turbulent wall pressure spectrum at subconvective wavenumbers and a suggested comprehensive model. Journal of Sound and Vibration 112, 125–147.

Ciappi, E., Magionesi, F., 2005. Characteristics of the turbulent boundary layer pressure spectra for high-speed vessels. Journal of Fluid and Structures 21, 321–333.

Ciappi, E., Magionesi, F., De Rosa, S., Franco, F., 2009. Hydrodynamic and hydroelastic analyses of a plate excited by the turbulent boundary layer. Journal of Fluid and Structures 25, 321–342.

Ciappi, E., Magionesi, F., De Rosa, S., Franco, F., 2012. Analysis of the scaling laws for the turbulence driven panel responses. Journal of Fluid and Structures 32, 90–103.

Cohen, E., Gloerfelt, X., 2018. Influence of pressure gradients on wall pressure beneath a turbulent boundary layer. Journal of Fluid Mechanics 838, 715–758.

Cook, R.K., Waterhouse, R., Berendt, R., Edelman, S., Thompson, M., 1955. Measurements of correlation coefficients in reverberant sound fields. Journal of the Acoustical Society of America 27, 1072–1077.

Corcos, G., 1964. The structure of the turbulent pressure field in boundary-layer flows. Journal of Fluid Mechanics 18, 353–378.

De Rosa, S., Franco, F., 2008a. Exact and numerical responses of a plate under a turbulent boundary layer excitation. Journal of Fluid and Structures 24, 212–230.

De Rosa, S., Franco, F., 2008b. A scaling procedure for the response of an isolated system with high modal overlap factor. Mechanical Systems and Signal Processing 22, 1549–1565.

Efimtsov, B., 1982. Characteristics of the field of turbulent wall pressure fluctuations at large Reynolds numbers. Sov Phys Acoust 30, 289–292.

Evans, N.D., Capone, D.E., Bonness, W.K., 2013. Low-wavenumber turbulent boundary layer wall-pressure measurements from vibration data over smooth and rough surfaces in pipe flows. Journal of Sound and Vibration 332, 3463–3473.

Fahy, F., 2003. Some applications of the reciprocity principle in experimental vibroacoustics. Acoustical Physics 49, 217–229.

Finnveden, S., Birgersson, F., Ross, U., Kremer, T., 2005. A model of wall pressure correlation for prediction of turbulence-induced vibration. Journal of Fluid and Structures 20, 1127–1143.

Franco, F., De Rosa, S., Ciappi, E., 2013. Numerical approximations of the predictive responses of plates under stochastic and convective loads. Journal of Fluid and Structures 42, 296–312.

Goody, M., 2004. Empirical spectra model of surface pressure fluctuations. American Institute of Aeronautics and Astronautics Journal 42.

Graham, W., 1997. A comparison of models for the wavenumber-frequency spectrum of turbulent boundary layer pressures. Journal of Sound and Vibration 206, 541–565.

Hambric, S.A., Hwang, Y., Bonness, W.K., 2004. Vibrations of plates with clamped and free edges excited by low-speed turbulent boundary layer flow. Journal of Fluid and Structures 19, 93–110.

Hwang, Y., Bonness, W.K., Stephen Hambric, S.A., 2009. Comparison of semi-empirical models for turbulent boundary layer wall pressure spectra. Journal of Sound and Vibration 319, 199–217.

Karimi, M., Croaker, P., Maxit, L., Robin, O., Skvortsov, A., Marburg, S., Kessissoglou, N., 2020. A hybrid numerical approach to predict the vibrational responses of panels excited by a turbulent boundary layer. Journal of Fluid and Structures 92.

Magionesi, F., Ciappi, E., Camussi, R., Pagliaroli, T., Di Mascio, A., Imperatore, B., Marino, A., 2012. Measurement and modeling of turbulent boundary layer excitation for naval and aeronautical applications, in: Noise and Vibration: Emerging Methods.

Marchetto, C., Maxit, L., Robin, O., Berry, A., 2018. Experimental prediction of the vibration response of panels under a turbulent boundary layer excitation from sensitivity functions. Journal of the Acoustical Society of America 143, 2954–2964.

Martin, N.C., Leehey, P., 1977. Low wavenumber wall pressure measurements using a rectangular membrane as a spatial filter. Journal of Sound and Vibration 52, 95–120.

Maury, C., Gardonoio, P., Elliott, S., 2002. A wavenumber approach to modelling the response of a randomly excited panel, part i: general theory. Journal of Sound and Vibration 252, 83–113.

Maxit, L., 2016. Simulation of the pressure field beneath a turbulent boundary layer using realizations of uncorrelated plane waves. Journal of the Acoustical Society of America 140, 1268–1285.

Maxit, L., Berton, M., Audoly, C., Juvé, D., 2015. Discussion about different methods for introducing the turbulent boundary layer excitation in vibroacoustics models, in: Flinovia - Flow Induced Noise and Vibration Issues and Aspects, Springer. pp. 249–278.

Maxit, L., Karimi, M., Meyer, V., Kessissoglou, N., 2020. Vibroacoustic responses of a heavy fluid loaded cylindrical shell excited by a turbulent boundary layer. Journal of Fluid and Structures 92.

Mellen, R.H., 1990. On modeling convective turbulence. Journal of the Acoustical Society of America 88, 2891–2893.

Palumbo, D., 2012. Determining correlation and coherence lengths in turbulent boundary layer flight data. Journal of Sound and Vibration 331, 3721–3737.

Rozenberg, Y., Robert, G., Moreau, S., 2012. Wall-pressure spectral model including the adverse pressure gradient effects. American Institute of Aeronautics and Astronautics Journal 50, 2168–2179.

Salze, E., Bailly, C., Marsden, O., Jondeau, E., Juvé, D., 2014. An experimental characterization of wall pressure wavevector-frequency spectra in the presence of pressure gradients, in: 20th AIAA/CEAS Aeroacoustics Conference.

Salze, E., Bailly, C., Marsden, O., Jondeau, E., Juvé, D., 2015. An experimental investigation of wall pressure fluctuations beneath pressure gradients, in: 21th AIAA/CEAS Aeroacoustics Conference.

Sanders, M., 2014. The Boundary Layer over a Flat Plate. Bachelor thesis. University of Twente.

Schloemer, R.H., 1967. Effects of pressure gradients on turbulent-boundary-layer wall-pressure fluctuations. Journal of the Acoustical Society of America 42, 93–113.

Smol'yakov, A., 2006. A new model for the cross spectrum and wavenumber-frequency spectrum of turbulent pressure fluctuations in a boundary layer. Acoustical Physics 52, 393–400.

Wittig, L., Sinha, A., 1975. Simulation of multicorrelated random processes using the fft algorithm. Journal of the Acoustical Society of America 58, 630–634.